Journal of Cleaner Production 571 (2026) 148813

Contents lists available at ScienceDirect

Journal of Cleaner Production

journal homepage: www.elsevier.com/locate/jclepro

# Reduced-energy processing of PLA/Talc biocomposites: Comparing in-mold crystallization and IR annealing

Hadi Saniei [a,b,*], Alberto Marcolongo [b], Marco Sorgato [a], Giovanni Lucchetta [a]

[a] Department of Industrial Engineering, University of Padova, Padova, Italy
[b] Sirmax SpA, Via Po 53, Mellaredo di Pianiga, VE, 30030, Italy

## HIGHLIGHTS

- High mold temperature increased crystallinity but required longer cooling.
- Low mold temperature shortened cycle time but reduced crystallinity.
- LM-IR restored crystallinity to the HM level after 1 min IR annealing.
- LM-IR reduced SEC and electricity cost by ~45% compared to HM.
- Scaling analysis confirmed LM-IR as the most energy-efficient route.

## ARTICLE INFO

*Keywords:*
PLA
Biocomposites
Crystallization
Injection molding
Energy efficiency
Specific energy consumption
Sustainable manufacturing

## ABSTRACT

PLA is a promising bio-based alternative to fossil-based plastics, but its slow crystallization during injection molding often requires high mold temperatures, increasing cycle time and energy demand. This study evaluates two manufacturing routes for obtaining highly crystalline PLA/talc injection-molded parts: (i) high mold temperature molding at 100 °C and (ii) low mold temperature molding at 30 °C followed by infrared post-molding annealing. The comparison integrates manufacturability, crystallinity, surface quality, thermomechanical/mechanical response, and gate-to-gate specific energy consumption. Samples molded at 100 °C with a cooling time of 35 s (HM(35)) reached a crystallinity of 54.12 ± 0.65%, whereas samples molded at 30 °C (LM) showed 25.0 ± 0.23%. A 1-min IR treatment increased the crystallinity of LM-IR to approximately 54%. Under optimized annealing utilization and similar crystallinity, LM-IR reduced specific energy consumption by about 45% relative to HM(35). Ejection force measurements showed lower ejection demand during the high mold temperature molding, while surface roughness parameters including Ra, Rz, Rv, and Rp showed lower values at 100 °C. Maximum tensile strength was 48.98 ± 0.42 MPa for LM, compared to 44.66 ± 1.44 MPa for HM(35) and 43.50 ± 0.83 MPa for LM-IR. Heat deflection temperature increased from 55.0 ± 0.2 °C for LM to 145.81 ± 0.42 °C for HM(35) and 134.6 ± 1.4 °C for LM-IR. Overall, the study provides an integrated gate-to-gate comparison of two established routes for the investigated commercial PLA/talc composite and quantifies the process-property-energy trade-offs that govern route selection in similar nucleated PLA systems.

## 1. Introduction

Recently, growing attention has focused on bio-based plastics such as polylactic acid (PLA), polyhydroxyalkanoates (PHA), and polybutylene succinate (PBS) as sustainable alternatives to conventional fossil-based polymers such as polyethylene (PE) and polypropylene (PP), driven by the finite nature of fossil resources and associated environmental concerns (Moshood et al., 2022; Singh et al., 2022; Spierling et al., 2018). Bioplastics are derived from bio-based sources, but they are not necessarily biodegradable. Among bioplastics, PLA has gained significant attention because it offers dual advantages: it is derived from bio-based, renewable sources and is also biodegradable, allowing composting under specific industrial conditions (Rojas et al., 2021; Swetha et al., 2023a, 2023b; Taib et al., 2023; Trivedi et al., 2023). While

* Corresponding author. Department of Industrial Engineering, University of Padova, Padova, Italy.
*E-mail addresses:* hadi.sanieisichani@phd.unipd.it (H. Saniei), amarcolongo@sirmax.com (A. Marcolongo), marco.sorgato@unipd.it (M. Sorgato), giovanni.lucchetta@unipd.it (G. Lucchetta).

https://doi.org/10.1016/j.jclepro.2026.148813
Received 19 January 2026; Received in revised form 19 May 2026; Accepted 18 June 2026
Available online 22 June 2026
0959-6526/© 2026 The Authors. Published by Elsevier Ltd. This is an open access article under the CC BY license (http://creativecommons.org/licenses/by/4.0/).

PLA is primarily used for short-shelf-life products, such as packaging, it also has potential for durable goods. However, to expand its application, PLA's mechanical and thermal properties need to be improved, which can be achieved through crystallization (Saeidlou et al., 2012).

Crystallization is the process by which polymer chains align into regular, repeating patterns, resulting in molecular order within the polymer structure. The degree of crystallinity is crucial for PLA's performance, influencing key properties such as stiffness, strength, heat resistance, and transparency (Bergström and Hayman, 2016; Saeidlou et al., 2012; Tan et al., 2016). The degree of crystallinity can be controlled by modifying material composition and/or optimizing processing conditions (Doroudiani et al., 1996; Fambri and Migliaresi, 2022; Farah et al., 2016; Mileva et al., 2018; Nagarajan et al., 2016). Despite PLA's advantages, its slow crystallization kinetics limit crystallization during processing. This limitation is pronounced under the short cooling times typical of injection molding, restricting its broader use in applications requiring high strength and heat resistance (De Santis et al., 2017; Nofar et al., 2011). Therefore, understanding the factors that affect crystallization and developing strategies to control it are essential for optimizing the properties of PLA products.

One effective way to control crystallinity and enhance PLA's performance is to incorporate nucleating agents, such as talc, calcium carbonate, zinc oxide, and carbon nanotubes, into the polymer matrix (Feng et al., 2018; Jiang et al., 2016; Zhao et al., 2023). These agents create nucleation sites that accelerate crystallization and promote the formation of well-ordered crystalline structures. As a result, both overall crystallinity and the material's mechanical properties and thermal stability improve (Gao and Masato, 2024; Wang et al., 2015). Among various nucleating agents, talc is a popular choice because of its cost-effectiveness and strong reinforcing properties (Gao and Masato, 2024; Kolstad, 1996; Li and Huneault, 2007; Yu et al., 2012). For instance, Shakoor et al. found that incorporating 5 wt% talc into PLA increased its crystallinity by up to 25%, significantly enhancing its mechanical properties and reducing crystallization half-times(Shakoor and Thomas, 2014). Relatively higher talc contents in PLA composites have also been investigated. For example, Lee et al. reported that PLA composites containing 30 wt% talc showed improved Young's modulus and thermal stability, whereas no further benefit was observed at 40 wt % because of agglomeration effects (Lee et al., 2020). In addition, Helanto et al. noted that talc loadings as high as 30 wt% have been reported to reinforce and toughen PLA (Helanto et al., 2021).

Another effective way to control the degree of crystallinity in PLA and enhance its properties is to optimize processing parameters. Among the various processing techniques for thermoplastics, injection molding stands out for its efficiency, scalability, and ability to produce complex shapes with high dimensional accuracy (Kashyap and Datta, 2015; Lim et al., 2008; Singh and Verma, 2017). Recent studies have highlighted the importance of process optimization, process monitoring, and tooling-related developments in injection molding for improving manufacturing efficiency and part quality (de Souza Marconi et al., 2025; Deng et al., 2025; Kitayama et al., 2025; Kuo et al., 2024, 2025; Oubellaouch et al., 2025; Rehman et al., 2025). Within this broad context, a key processing factor governing crystallization is mold temperature, which significantly influences PLA crystallization behavior (De Santis et al., 2017). Using a high mold temperature above PLA's glass transition temperature ($T_g$) slows cooling, giving polymer chains more time to align into well-ordered crystalline structures. This results in higher crystallinity, improving the material's stiffness, strength, and heat resistance. However, slower cooling can lead to longer cycle times ($t_c$), thereby reducing production efficiency.

In contrast, using a low mold temperature (below $T_g$) increases the cooling rate, enabling faster solidification and a shorter $t_c$. This improves production efficiency and can reduce energy use during molding. However, rapid cooling limits polymer chain mobility, resulting in lower crystallinity and reduced mechanical strength and thermal resistance. As a result, low mold temperature molded samples often require post-molding annealing to further enhance their crystalline structure and improve their mechanical and thermal properties.

Annealing involves heating a molded part to a temperature above its $T_g$ but below its melting point, allowing polymer chains to rearrange into more ordered crystalline structures. Thermal annealing methods such as microwave heating (De Santis et al., 2017;Seok et al., 2023), oven heating (Butt and Bhaskar, 2020; Costa et al., 2023; Ivey et al., 2017; Sudin, 2024), air dryer heating (Wach et al., 2018), and infrared (IR) heating (Lee et al., 2021) are commonly used to increase crystallinity during or after processing. Because annealing can be performed offline and in batches, it can redistribute the energy demand per part and help compensate for the limited crystallization achieved during low mold temperature molding, thereby improving suitability for higher-performance applications. However, in industrial implementation, these advantages may depend on practical factors such as the available floor space for the annealing unit, the required buffer capacity between molding and post-treatment, the ease of line integration, and the extent to which batch handling and annealing residence time limit overall throughput.

Energy performance is a key sustainability lever in injection molding and is typically reported as specific energy consumption (SEC, kWh/kg). SEC is then translated into climate and cost indicators using the electricity-mix emission factor (kg $CO_2$e/kWh) and the tariff (€/kWh). Life-cycle inventories (LCIs) often adopt a single reference of 1.47 kWh/kg for molding 1 kg of thermoplastic, but this simplification can misrepresent real operations because SEC varies with machine efficiency, utilization ($\eta$), throughput, and material (P and O, n.d.). Elduque et al. developed an empirical model capturing these dependencies and reported large deviations from the fixed LCI value (Elduque et al., 2018). Lucchetta et al. measured 0.40 kWh/kg for an all-electric injection molding machine versus 0.65 - 0.83 kWh/kg for comparable hydraulic machines, and showed that cooling/process optimization (e.g., lower hot-runner/nozzle temperatures; reduced coolant flow with series channeling) cuts energy without compromising quality (Lucchetta et al., 2018). Thiriez & Gutowski highlighted that, at the press-only level, SEC for all-electric machines is approximately constant with respect to throughput, whereas including auxiliaries and plant losses raises system-level figures, explaining why some studies report higher values (Thiriez and Gutowski, 2006).

This study evaluates two PLA crystallization methods during processing, including high mold temperature molding and low mold temperature molding followed by post-molding IR annealing, within a gate-to-gate boundary, assessing crystallinity, manufacturability, part quality, energy efficiency, and electricity-related operating-cost indicators. For this evaluation, box-shaped samples were produced at two distinct mold temperatures: one above PLA's glass transition temperature ($T_g$) at 100 °C and one below $T_g$ at 30 °C, followed by IR post-molding annealing. IR irradiation was selected for its rapid, uniform, contactless heating, enabling precise temperature control and minimizing deformation risk, and for its potential energy efficiency and selective heating of target regions (Cheng et al., 2025; Wang et al., 2024). The assessment of crystallinity, ejection force, thermomechanical behavior, surface roughness, and gate-to-gate sustainability indicators including SEC, $CO_2$ emissions ($CO_2$e), and electricity costs were conducted to compare the two routes under the selected system boundary. While mold-temperature-assisted crystallization, post-molding annealing, and process-energy analysis are individually established topics, direct side-by-side comparisons between high mold temperature molding and low mold temperature molding followed by IR annealing under the same material and geometry framework remain limited. The contribution of the present study therefore lies in establishing a controlled gate-to-gate comparison of two competing processing routes for PLA/talc parts within a single experimental framework and at comparable final crystallinity. This design makes it possible to quantify how the route used to generate crystallinity affects manufacturability, surface quality, thermomechanical/mechanical response, and process energy, thereby

providing process-level insight for reduced-energy route selection in nucleated PLA systems.

## 2. Materials and methods

### 2.1. PLA characterization

A commercial PLA/talc composite grade, IM2368, supplied by Sirmax S.p.A., was used in this study. The material consists of 70 wt% PLA, 29 wt% talc, and 1 wt% processing agents. Because only this single industrially relevant commercial formulation was investigated, the results of the present work should be considered formulation-specific. Accordingly, the study was designed to compare the two processing routes on a representative nucleated PLA compound rather than to establish universally generalizable quantitative relationships for all PLA grades or nucleating systems. The main properties of the composite are reported in Table 1.

#### 2.1.1. Modulated differential scanning calorimetry (MDSC)

The thermal properties and crystallinity of the samples were evaluated using the modulated differential scanning calorimeter (MDSC) method on a DSC-Q2000 from TA Instruments. Each sample was heated from room temperature to 225 °C at 2 °C/min, with a modulation amplitude of ±1 °C and a modulation period of 60 s. The degree of crystallinity was calculated using Equation (1) after determining the areas under the melting peak in the reversing heat flow and the cold crystallization peak in the non-reversing heat flow.

$$X_c = \frac{\Delta H_m - \Delta H_{cc}}{\omega_{PLA} \times \Delta H_m^*} \times 100 \quad (1)$$

where $\omega_{PLA}$ is the weight fraction of PLA in the composite, $\Delta H_m$ and $\Delta H_{cc}$ are the heat enthalpies of melting and cold crystallization, respectively. $\Delta H_m^*$ is the heat of fusion required to melt 100% crystalline PLA, which is 93.6 J/g (Fischer et al., 1973). The crystallinity of the samples was evaluated at the same predefined location for all specimens to ensure consistency and comparability. The MDSC measurements were used to quantify the final crystalline state of the processed samples after molding and/or annealing. They were not designed to provide time-resolved crystallization data and therefore were not used for formal kinetic fitting. Moreover, the through-thickness crystallinity distribution was assessed using microtomed sections, and variability among layers was evaluated based on the standard deviation.

#### 2.1.2. Dynamic Mechanical Analysis (DMA)

The dynamic mechanical properties of the samples were evaluated by Dynamic Mechanical Analysis (DMA) using a DMA 242 Artemis (NETZSCH) in a three-point bending configuration. Rectangular specimens measuring 40 × 11 × 2 mm were tested. Measurements were performed over a temperature range of 10 °C to 120 °C at a heating rate of 3 K/min, with a load frequency of 1 Hz and an oscillation amplitude of 15 μm. Test parameters were selected in accordance with ASTM D5023. The storage modulus ($E'$) was determined at 30 °C and 100 °C.

**Table 1**
Main properties of the PLA/Talc composite.

| Properties | Method | Unit | Value |
|---|---|---|---|
| Melt Flow Rate [190 °C – 2.16 kg] | ISO 1133 | g/10′ | 25 |
| Density at 23 °C | ISO 1183 | g/cm$^3$ | 1.45 |
| Glass transition temperature | ISO 11357-1 | °C | 56 |
| Mold Shrinkage | ASTM D955 | % | 0.1 – 0.5 |
| HDT, B (0.45 MPa) | ISO 75-1 | °C | 50 |
| Melting Temperature | ISO 11357-1 | °C | 170 |

### 2.2. Sample preparation and characterization

#### 2.2.1. Injection molding process setup

A hollow, box-shaped sample with two drafted walls, as schematically illustrated in Fig. 1, was produced using a micro injection molding machine (Wittmann Battenfeld, MicroPower 15). Fig. 1 also shows the mold assembly, which is based on a Hasco modular system. The mold temperature was set and controlled using four electrical cartridge heaters (two per mold half) in combination with two thermocouples to ensure stable thermal conditions. To achieve different levels of crystallinity, two mold temperatures were selected: 100 °C (high mold temperature) and 30 °C (low mold temperature). For the low mold temperature molding, the active cooling system (e.g., water cooling) was turned off; due to the small mold size, the temperature was maintained through passive heat dissipation to the surrounding air and monitored during processing using thermocouples. These thermocouple readings were used to verify the imposed mold-temperature boundary conditions during processing; however, they did not provide direct temperature measurements inside the molded part. The fabricated samples were labeled LM, HM(cooling time), and LM-IR, corresponding to low mold temperature molding, high mold temperature molding with a specified cooling time (expressed in seconds), and low mold temperature molding followed by IR annealing, respectively. Before injection molding, the material pellets were dried in a hot air dryer at 80 °C for 4 h. The processing parameters were set as follows: barrel temperature of 200 °C, holding pressure of 120 bar, holding time of 5 s, and cooling time varied according to the selected mold temperature condition.

#### 2.2.2. Ejection force and roughness evaluation

The ejection force of the molded samples was measured using a Kistler 9223A piezoelectric force sensor mounted beneath the ejector system. Six cylindrical ejector pins with a 1 mm tip diameter were arranged symmetrically around the part to provide balanced force distribution during demolding and to minimize part deformation. The ejector pins transferred the applied load through a force distribution plate to the piezoelectric sensor, as illustrated in Fig. 2. To ensure reliable measurements, data acquisition was started only after the molding process and the force-monitoring system stabilized, following the production of 20 preliminary samples.

The surface topography of the molded samples was evaluated using a Sensofar S-Neox imaging confocal microscope, while the acquired data were processed using SensoVIEW software. Roughness measurements were carried out on the inner surface of the molded parts, and the parameters Ra, Rz, Rv, and Rp were determined in accordance with ISO 4287/4288. An S-L filter with cutoff values of $\lambda_S = 2.5$ μm and $\lambda_L = 80$ μm was applied prior to the roughness analysis. The surface morphology of the injection-molded samples was evaluated using FEI Quanta 450 scanning electron microscope (SEM).

#### 2.2.3. IR annealing

The annealing process was conducted using an IR heating apparatus (Krelus, Switzerland) with a maximum power output of 3400 W. To ensure uniform heat distribution and prevent warpage or deformation, a small rotary plate continuously rotated the samples during annealing. The IR heater was operated at constant maximum power to enable rapid heating, and a parametric study was conducted by varying the source-sample distance. The objective was to identify processing conditions that allow the samples to reach the target annealing temperature (~85 °C) within the shortest possible time while preventing thermal degradation, such as burning or distortion. Surface temperature was monitored using a pyrometer. The target temperature was selected within the cold-crystallization temperature ($T_{cc}$) range of the material, as determined by differential scanning calorimetry (MDSC), to promote isothermal cold crystallization. Based on the parametric evaluation, a source-sample distance of 15 cm was identified as the optimal condition. Distances below this threshold resulted in localized overheating and

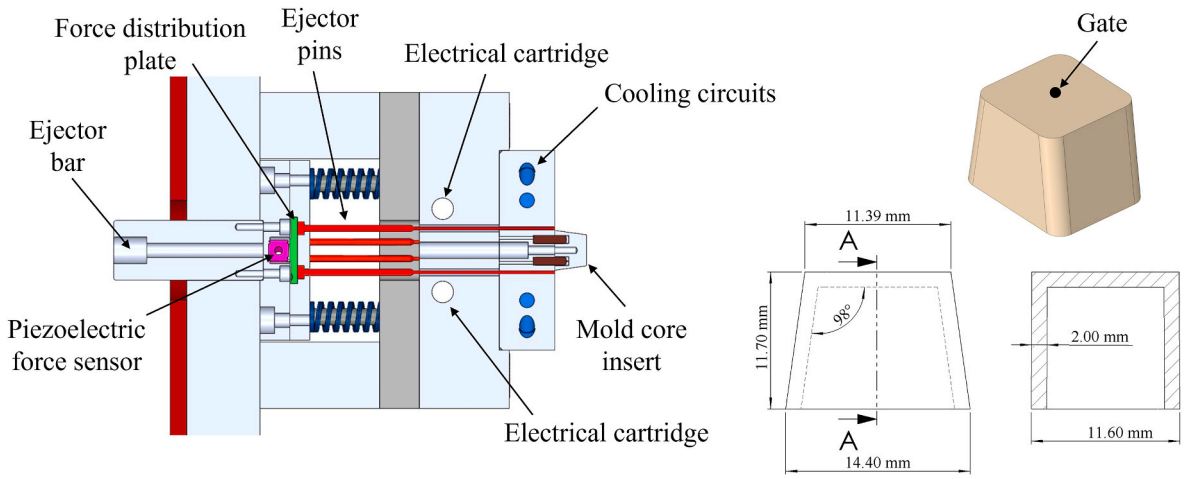


**Fig. 1.** Mold assembly and schematic drawing of the molded sample.

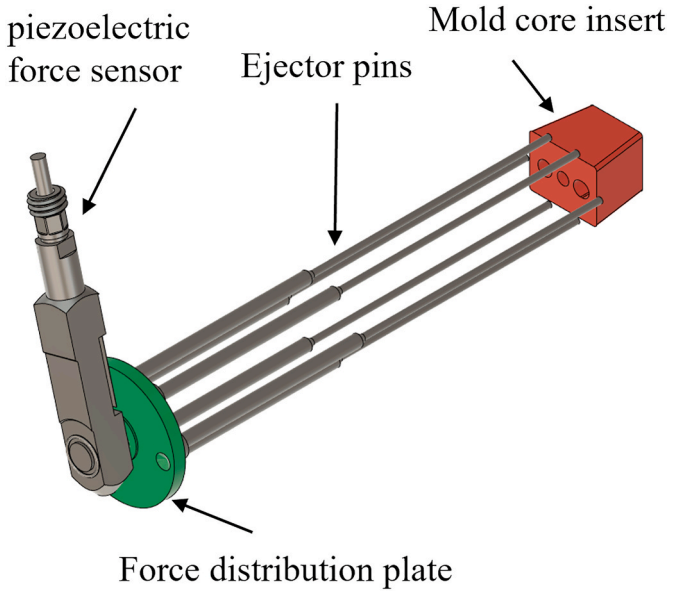


**Fig. 2.** Schematic of the ejection force measurement setup (Maciariello, 2024).

sample deformation, whereas larger distances led to slower heating rates and prolonged processing times. A schematic representation of the annealing setup is provided in Fig. 3.

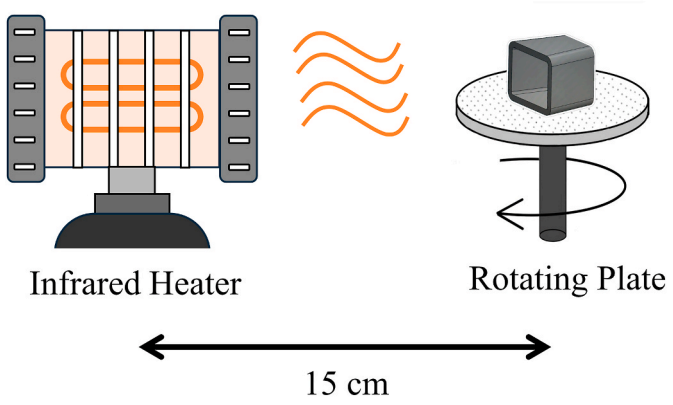


**Fig. 3.** Schematic of the annealing process.

#### 2.2.4. Tensile and heat deflection temperature (HDT) tests

Because the original box-shaped samples were too small to prepare standardized tensile and HDT specimens directly, separate standard dog-bone and rectangular specimens were molded for tensile and HDT testing. These specimens were produced under processing conditions corresponding to the HM(35), LM, and LM-IR samples, with crystallinity levels comparable to those of the corresponding box-shaped samples, thereby enabling a relative comparison of tensile and thermomechanical trends. Furthermore, the through-thickness crystallinity gradient was assessed by sectioning the specimens into thin layers using a microtome, in order to verify that the crystallinity distribution across the thickness was within a comparable and acceptable range among the different samples. Uniaxial tensile tests were conducted at room temperature according to ISO 527-2 using Type 1A dog-bone specimens with a thickness of 4 mm. Tests were performed on an Instron 3366 universal testing machine equipped with a 5 kN load cell at a crosshead speed of 5 mm/min, and Young's modulus was determined using an extensometer.

Heat deflection temperature (HDT) was determined using an Instron CEAST HV6M system in accordance with ISO 75, Method B (0.45 MPa). Rectangular specimens with dimensions of 80 × 10 × 4 mm were tested in the flatwise position under three-point bending configuration. During testing, the specimens were immersed in a silicone oil bath and subjected to a flexural stress of 0.45 MPa at the midpoint. The temperature of the oil bath was increased at a constant rate of 2 °C/min, and the test was terminated when the specimen reached a deflection of 0.34 mm. The temperature recorded at this point was taken as the HDT value.

### 2.3. Numerical simulation

A Temperature Profile Study was performed using Autodesk Moldflow Synergy, version 2026, as part of a numerical simulation of the injection molding process, in order to predict and track the temperature distribution across the sample thickness and the bulk temperature during cooling. The CAD geometry of the test specimens was imported in STEP format and meshed with a dual-domain triangular surface mesh consisting of 26,518 elements with an average in-plane element size of approximately 0.2 mm, an average aspect ratio of 1.52, and a match percentage of 94%. The simulation was run using the "Cool + Fill + Pack" sequence. To run the simulation, the material's rheological, thermal, and mechanical properties were set based on the software database. The mold surface temperatures were set to 30 °C and 100 °C, respectively. The simulation tracked the temperature gradient across the sample thickness and the temperature evolution at the core and surface during the cooling phase and at the time of ejection. The Moldflow results were used primarily to provide comparative insight into the

relative thermal histories of the LM and HM conditions and to support the interpretation of shrinkage and ejection behavior. The imposed mold-temperature boundary conditions were experimentally controlled and monitored by thermocouples during processing. However, direct experimental validation of the predicted in-part temperature fields (e.g., by embedded thermocouples or IR thermography) was not performed in the present study. Accordingly, the simulated temperature fields are interpreted here in a qualitative/comparative sense rather than as fully validated absolute temperature measurements.

### 2.4. Energy consumption and climate impact

#### 2.4.1. Energy consumption measurements

The gate-to-gate electrical energy demand of the two processing approaches to achieve a similar degree of crystallinity in the samples was quantified by monitoring the cycle time and power during both processes. For the injection molding step, signals were collected at 1 Hz using a DIRIS A-10 three-phase energy meter (Socomec, Italy) connected to the injection molding machine and to a PC via RS-485. Data acquisition was managed using the open-source Python library MinimalModbus. At the start of the measurement, the injection molding machine heat-up phase was complete, and the temperatures of each barrel zone and the mold had already reached their set values. Accordingly, the present energy analysis was limited to the gate-to-gate electrical demand of the monitored molding cycle and the IR annealing step under steady-state operating conditions. Upstream and facility-level contributions were not included, such as machine start-up and warm-up, compressed-air generation, material drying beyond the pre-drying step required before processing, and broader plant-level losses or services (e.g., ventilation, distribution losses, and general utilities). The purpose of this boundary was to enable a consistent comparative assessment of the two processing routes under controlled laboratory conditions. The electrical energy consumption of the molding cycle for the HM and LM samples ($E_{Molding}$) was calculated using Equation (2):

$$E_{Molding}\ [Wh] = P[W] \times t_c\ [h] \tag{2}$$

where $P$ is the active power and $t_c$ is the injection molding cycle time. To verify the reliability of the results, additional measurements were taken for larger injection molding cycles (5, 15, and 30 samples), and the total energy consumption was normalized by the number of samples to obtain the energy per part. For the IR annealing step, electrical current ($I$) was measured using an ESP32 microcontroller paired with an LEM TT 50-SD current transformer, and data acquisition was performed using the open-source Python library MinimalModbus. The energy consumption during IR annealing ($E_{IR}$) was calculated using Equations (3) and (4):

$$P_{IR} = I\ [A] \times 220\ [V] \tag{3}$$

$$E_{IR}\ [Wh] = P_{IR}\ [W] \times t_{c,IR}\ [h] \tag{4}$$

where $P_{IR}$ is the power, $I$ is the electrical current, and $t_{c,IR}$ is the IR annealing time. Energy consumption for different numbers of samples per batch ($N_{batch}$: 1, 5, 15, 30) during annealing was also calculated to evaluate the effect of the number of parts per batch by distributing the batch energy across the parts.

#### 2.4.2. Specific energy consumption, electricity cost, and $CO_2$ emission

The SEC for the two processing methods was calculated using Equation (5):

$$SEC\ [kWh/kg] = \frac{E\ [kWh]}{m\ [kg]} \tag{5}$$

where $m$ is the mass of the HM or LM samples, calculated to be approximately 1 g. Because the investigated parts were in the micro-injection range (m ≈ 1 g), the calculated SEC values are particularly sensitive to the distribution of fixed machine and tooling loads over a very small processed mass. Therefore, the absolute SEC values reported here are specific to the present experimental scale and should not be directly transferred to larger conventional injection-molded components. In the present study, SEC was calculated on the basis of the measured gate-to-gate electrical demand only; therefore, it does not represent a full-plant or life-cycle energy indicator. The energy costs of processing per kg of material for the two processing methods were calculated using Equation (6):

$$Price_{kg} = P_e\ (€) \times SEC\ [kWh] \tag{6}$$

where $P_e$ is the unit electricity price, set to $P_e = 0.1899$ €/kWh, as reported by the EU for non-household consumers in the second half of 2024. The cost indicator considered in this study is limited to electricity expenditure associated with the measured gate-to-gate process energy. It does not include capital expenditure, maintenance, equipment depreciation, labor, floor-space, handling, automation, or other plant-specific overheads associated with adding an IR annealing step. Accordingly, the reported values should be interpreted as comparative electricity-cost indicators rather than as a complete techno-economic assessment of the two routes. The amount of $CO_2$ emissions from electricity consumption can be calculated using Equation (7) (Kocabey Çiftçi and Özceylan, 2025; Psomopoulos et al., 2010):

$$CO_2e[kg] = E[kWh] \times EF_{CO_2}[kgCO_2e/kWh] \tag{7}$$

where $EF_{CO_2}$ is the $CO_2$ emission factor, a coefficient representing the amount of $CO_2$ emitted per kilowatt-hour of electricity consumed. In this study, the EU-27 average emission factor $EF_{CO_2}$ of 0.2883 kg $CO_2$e/kWh was used as a reference value for comparative purposes between the two processing routes (Balaras et al., 2023).

### 2.5. Statistical analysis

All measurements were repeated multiple times (n ≥ 3 depending on the experiment), and the results are reported as mean ± standard deviation (SD). Error bars in the figures represent the standard deviation of the measurements. Statistical analysis was performed using one-way analysis of variance (ANOVA) to evaluate differences between experimental conditions. Differences were considered statistically significant at a confidence level of 95% ($p < 0.05$).

## 3. Results and discussion

### 3.1. MDSC analysis

MDSC is a thermal analysis technique in which a sinusoidal temperature modulation is superimposed on a constant heating rate to separate heat flow components that are responsive and unresponsive to temperature changes. This allows distinguishing between reversible events, such as the glass transition, and irreversible events, such as crystallization. By isolating these two heat flow signals, MDSC enables a more accurate interpretation of overlapping thermal transitions. Fig. 4 shows the MDSC heat flow, as well as the reversing and non-reversing heat flow signals for LM, HM(35), and LM-IR.

As shown in Fig. 4(a), the MDSC thermogram of the LM sample exhibited an exothermic peak at approximately 78.99 °C in the non-rev heat flow, indicating cold crystallization. This process occurs as polymer chains, initially trapped in an amorphous state due to rapid cooling, rearrange into crystalline structures during reheating, releasing heat in the process. The presence of this peak suggested that only limited crystallization developed during molding, emphasizing the effect of the low mold temperature. Consistent with this behavior, the LM sample exhibited a low crystallinity of approximately 25.0 ± 0.23%.

As shown in Fig. 4(b), the MDSC thermogram of HM(35) shows a significant endothermic peak at 173.62 °C in the non-reversing heat

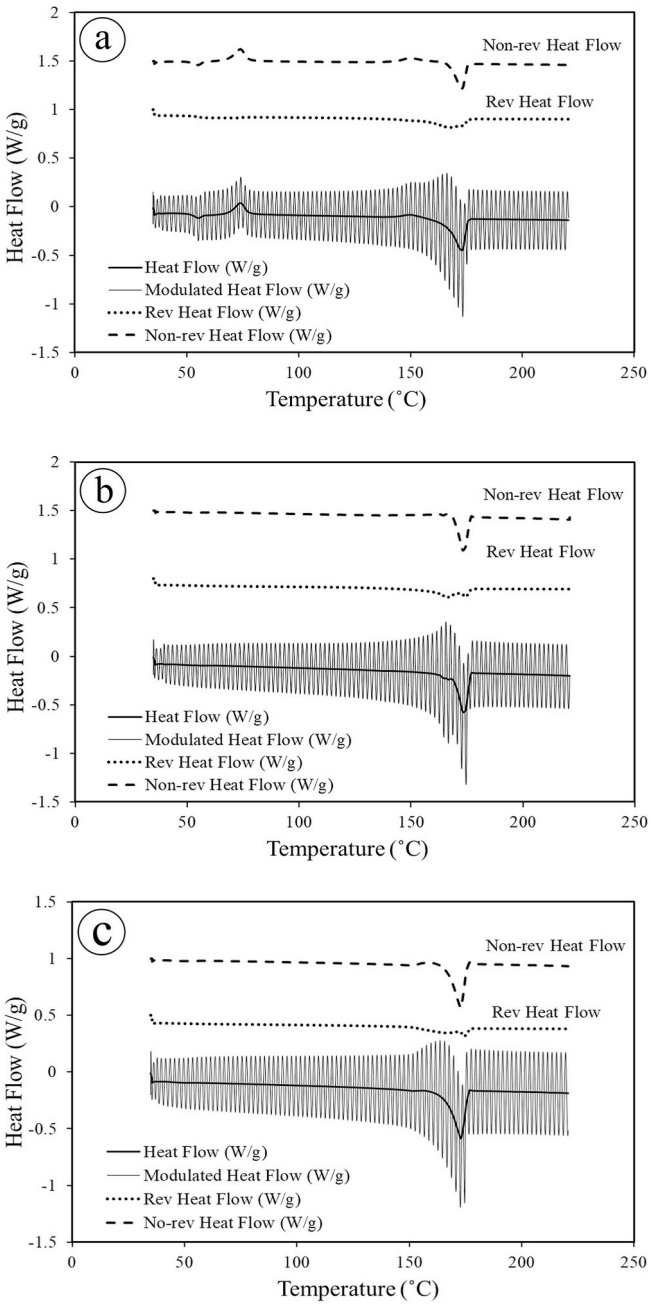


**Fig. 4.** Modulated heat flow, non-reversing heat flow, and reversing heat flow of the (a) LM, (b) HM(35), and (c) LM-IR, during the first heating scan.

flow, corresponding to the melting of the material. In contrast, the absence of a cold crystallization peak indicates that crystallization occurred isothermally in the high mold temperature molding after 35 s, allowing the sample to reach the highest crystallinity measured in this study of approximately 54.12 ± 0.65%. Moreover, two endothermic peaks at 165.56 °C and 173.62 °C were observed in the reversing heat flow, which are attributed to the melting of different crystalline phases within the sample (Jain et al., 2012).

IR annealing was applied to the LM samples to compensate for the limited crystallization achieved during low mold temperature molding. Based on the MDSC thermogram of the LM sample, the cold-crystallization peak was observed over the temperature range of approximately 70 °C to 85 °C, with the exothermic event ending near 85 °C. Therefore, an annealing temperature of about 85 °C was selected, which lies at the upper end of the cold-crystallization interval, where sufficient molecular mobility is available to promote efficient crystal development (Tábi et al., 2016). Other annealing temperatures within this range, as well as temperatures above 85 °C, were also examined. The results showed that annealing at lower temperatures within the 70 °C to 85 °C interval was feasible, but a longer treatment time was required to reach the target crystallinity similar to HM. In contrast, temperatures above 85 °C were not preferred because they made the IR annealing process more difficult to control and increased the risk of non-uniform heating, localized overheating, and dimensional distortion of the samples. The results showed that, under the selected annealing conditions, 1 min of IR annealing was sufficient to promote substantial post-molding crystallization. This is confirmed by the MDSC thermogram of the LM-IR sample shown in Fig. 4(c), where the pronounced cold-crystallization peak observed for the LM sample was no longer evident. This behavior indicates that most of the crystallization had already occurred during the IR treatment. As a result, the crystallinity of the LM-IR sample increased to approximately 54%, similar to the value measured for HM (35) (54.12 ± 0.65%), confirming that IR annealing effectively shifted crystallization from the molding stage to a short post-molding step. Moreover, microtome-section MDSC showed only negligible core-to-surface crystallinity variation (within the experimental SD), indicating that the measured crystallinity values are representative of the specimen thickness. Since crystallinity non-uniformity may influence barrier performance, degradation behavior, and dimensional stability during service, this aspect may have potential implications for applications where these properties are critical, such as food packaging.

Fig. 5 shows the crystallinity of HM and LM samples as a function of cooling time. The results indicate that the high mold temperature molding produced higher crystallinity, ranging from 46.33 ± 0.14% at 15 s to 54.12 ± 0.65% at 35 s. In contrast, the low mold temperature molding generated significantly lower crystallinity, around 25 ± 0.23%, regardless of cooling time. During PLA injection molding, maintaining the mold temperature between the glass transition temperature and the melting temperature ($T_m$) facilitates isothermal melt crystallization by allowing polymer chains to remain mobile and rearrange into ordered crystalline structures while held at a constant temperature. The increase in crystallinity with longer residence times during high mold temperature molding qualitatively highlights the dependence of crystallization on cooling time within the experimental window investigated.

The present discussion is intentionally limited to a qualitative interpretation of this trend. Although kinetic models such as Avrami-type approaches can provide deeper mechanistic and predictive insight into PLA crystallization, they were not applied here because the

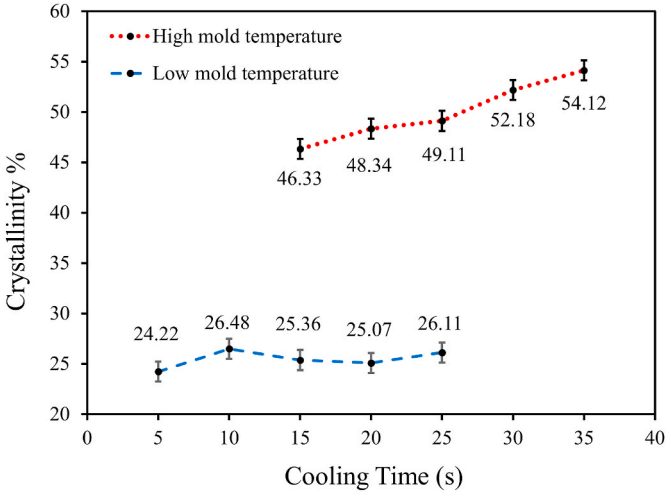


**Fig. 5.** Crystallization degree of the HM and LM samples as a function of cooling time (values of mean ± SD, n = 3).

current dataset was not generated from dedicated time-resolved crystallization experiments. Instead, it consists of endpoint crystallinity values measured after processing under complex, predominantly non-isothermal thermal histories during molding and after post-molding IR treatment, and only a discrete set of residence/cooling times was investigated. Under these conditions, applying a simplified kinetic fit could over-interpret the data. A dedicated study combining time-resolved temperature and crystallinity measurements with appropriate isothermal or non-isothermal kinetic modeling would be required to quantitatively describe crystallization during the present processing routes.

### 3.2. Ejection force and roughness evaluation

Fig. 6 compares the ejection forces of the samples molded at 100 °C and 30 °C. As shown in Fig. 6, higher ejection forces of around 101 N were recorded for LM samples, and these values remained unchanged across the different cooling times. By contrast, the HM sample required much lower forces to eject.

Fig. 6 shows that the LM samples required a much shorter cooling time to reach suitable ejection conditions than the HM samples. In fact, the cooling time for the LM samples could be reduced to about 5 s, enabling significantly earlier demolding, a shorter $t_c$, and faster production. HM samples need to stay in the mold longer to cool and contract enough to detach from the cavity plate and adhere to the core plate of the mold. Fig. 6 also shows that lower ejection forces were required during the high mold temperature molding than during the low mold temperature molding. Two factors contribute to the lower recorded ejection forces under the high mold temperature molding.

The first factor is related to part contraction at ejection. During injection molding, thermal shrinkage is necessary for the part to be ejected from the cavity plate (the fixed half) and to adhere to the core plate (the moving half), so that the part remains on the side equipped with ejectors. Thermal shrinkage occurs in all polymers, whether amorphous or semi-crystalline; however, in semi-crystalline polymers - as in the material investigated in this study - it can be further increased by crystallization. This crystallization-induced shrinkage is time-dependent, since it does not occur instantaneously but follows a kinetic process governed by temperature. To clarify how these thermally driven phenomena evolve during the molding cycle, numerical simulations were performed to estimate the temperature history of the samples. Because direct experimental validation of the predicted in-part temperature fields was not available, the simulation results are used here primarily to support the qualitative interpretation of the relative thermal histories of the two

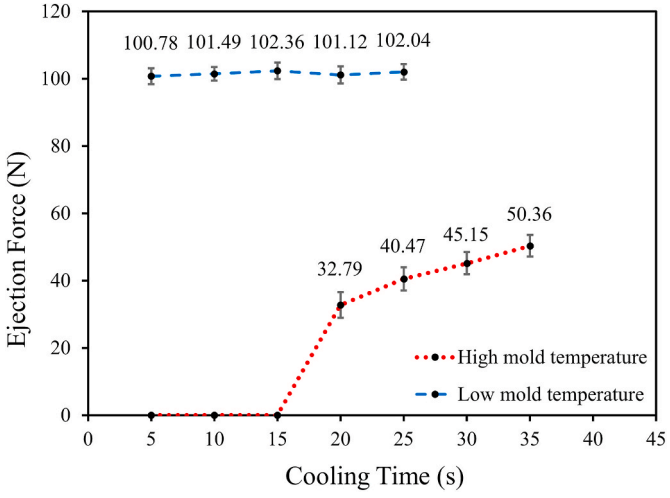


**Fig. 6.** Ejection force of HM and LM samples as a function of cooling time (values of mean ± SD, n = 10).

molding conditions rather than to establish the exact absolute temperature field. Fig. 7(a) and (b) show the simulated temperature gradients across the thickness of the LM and HM samples, respectively, at the beginning of the cooling phase, while Fig. 7(c) and (d) illustrate the simulated temperature evolution at the core of the LM and HM samples during the cycle. In this sense, the simulations provide comparative insight into how the temperature distribution evolves over time and how the two molding conditions differ in terms of shrinkage and ejection behavior.

As shown in Fig. 7(a) and (b), at the start of the cooling phase, the core temperatures were higher than the surface temperatures in both samples. The simulated average temperature in the LM case was around 115 °C, whereas in the HM case it was about 165 °C, indicating that the LM component was already more contracted than the HM one. Fig. 7(c) and (d) further indicate that, in the simulations, by the end of the cycles the core temperatures had approached the mold temperatures in both conditions, yielding bulk temperatures of ~30 °C for LM and ~100 °C for HM. According to the simulated thermal histories, the HM sample remained at a higher temperature than the LM sample at demolding and therefore likely underwent less thermal contraction, which would favor detachment from the core side and contribute to the lower ejection forces observed under high mold temperature molding. Conversely, the lower simulated temperature of the LM sample suggests greater contraction, increasing the normal force on the core and, in turn, the friction that the ejectors had to overcome. The ejection force results revealed that nearly 20 s are required before the HM part can be ejected. In the simulations, by that time (see Fig. 7(d)), the part core had already approached the mold temperature and remained near 100 °C for several seconds. This suggests that the additional shrinkage observed in this interval is more plausibly associated with ongoing crystallization than with further cooling, since the simulated temperature field changes only modestly in this stage. Consistent with this interpretation, Fig. 6 shows that, for HM, increasing the cooling time beyond 20 s led to higher ejection forces, which is compatible with additional shrinkage associated with continued crystallization. Consequently, the observed increase in ejection force is more likely related to increased normal and frictional forces on the core than to further thermal contraction alone.

In addition to the shrinkage-related effect discussed above, the ejection force is also influenced by the mechanical state of the polymer at demolding. The second key factor influencing the ejection force is the storage modulus, $E'$ (Masato et al., 2018, 2021). Fig. 8 shows the results of DMA analysis performed to evaluate the storage modulus of HM samples at around 100 °C and LM samples at around 30 °C. As shown in Fig. 8, under high mold temperature molding, where the temperature exceeds PLA's glass transition temperature ($T_g$ ~ 65 °C), the material remained in a relatively rubbery state at the time of ejection, exhibiting a lower $E'$ at approximately 300 MPa. In contrast, under the low mold temperature molding at 30 °C (well below $T_g$), the material was in a glassy state, resulting in a higher $E'$.

Mechanistically, the ejection force can be written as $F_e = \mu F_N$, where $F_N$ is the normal load generated by shrinkage on the core, and $\mu$ is the static friction coefficient. In simple core-ring geometries, $F_N$ scales with the radial shrinkage strain of the ring and with the elastic response of the polymer, providing a direct route by which a higher $E'$ increases $F_N$ (and thus $F_e$) for a given contraction (Maciariello, 2024; Pontes and Pouzada, 2004). The LM parts are ejected at a lower temperature (glassy state), so for a given contraction, they develop a larger normal load because $E'$ is higher. Consequently, the ejection force reflects a combined effect of (i) the normal pressure generated by shrinkage and (ii) the elastic response, since the normal force scales with the product of the shrinkage-induced deformation and the elastic modulus $E'$ (Pontes and Pouzada, 2004).

### 3.3. Roughness evaluation

Table 2 compares the surface roughness of the HM and LM samples using the roughness parameters including Ra, Rz, Rv and Rp. The results

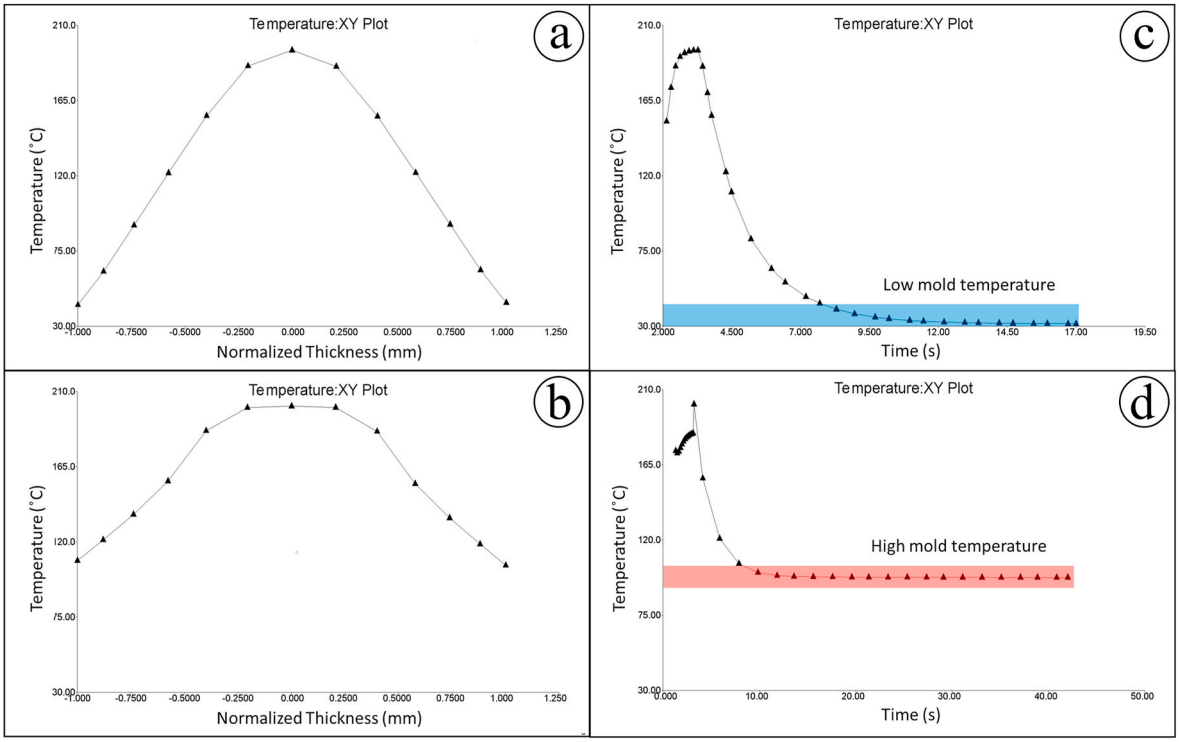


**Fig. 7.** Temperature profiles from the cooling simulation of the two molding conditions obtained from the numerical simulations of the process: (a) and (b) temperature profiles through the thickness of the LM and HM samples, respectively; (c) and (d) temperature evolution at the core of the LM and HM samples, respectively.

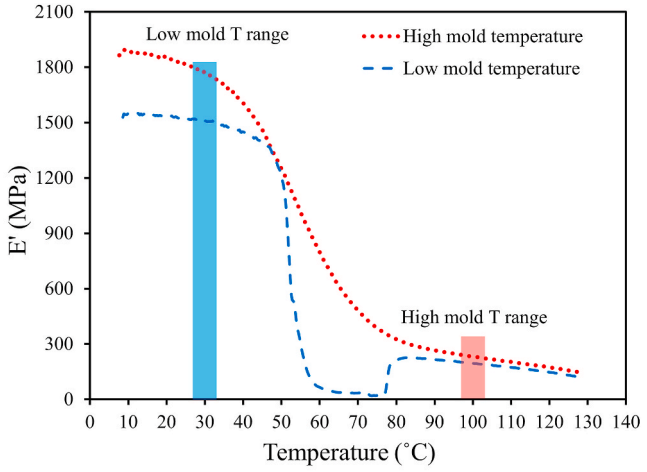


**Fig. 8.** Storage modulus of HM and LM samples as a function of temperature.

revealed lower roughness values for the HM compared to LM samples. As shown in Table 2, lower Ra values for the HM, ranging from 0.101 ± 0.014 μm to 0.143 ± 0.037 μm were measured over the investigated cooling times, whereas the LM samples exhibited higher Ra values, ranging from 0.249 ± 0.020 μm to 0.256 ± 0.023 μm. The results of Table 2 showed that within each processing route, cooling time did not significantly affect the roughness parameters. The high mold temperature molding produced smoother surfaces than the low mold temperature molding.

The surface roughness of an injection molded part is significantly influenced by the mold temperature (Gülçür et al., 2025; Maciariello, 2024; Sorgato et al., 2017). Higher mold temperatures result in smoother surfaces when the mold itself is smooth due to several factors. Firstly, higher mold temperatures result in a better replication of the mold surface. When the mold is heated, the plastic melt can pack out against the mold surface more effectively, ensuring that the fine details of the mold are accurately transferred to the molded part. This results in a smoother surface finish on the part. Additionally, at higher temperatures, the plastic melt remains less viscous for a longer period. This lower viscosity allows the melt to flow more easily into the small

**Table 2**
Surface roughness parameters (Ra, Rz, Rv and Rp) of LM and HM samples as a function of cooling time (mean ± SD, n = 5).

| Sample | Cooling Times (s) | Roughness parameter (μm) | | | |
|---|---|---|---|---|---|
| | | Ra | Rz | Rv | Rp |
| LM | 5 | 0.249 ± 0.020 | 2.673 ± 0.228 | 1.458 ± 0.196 | 1.214 ± 0.187 |
| | 10 | 0.256 ± 0.023 | 2.741 ± 0.236 | 1.503 ± 0.208 | 1.238 ± 0.195 |
| | 15 | 0.251 ± 0.021 | 2.695 ± 0.231 | 1.471 ± 0.201 | 1.223 ± 0.191 |
| HM | 15 | 0.101 ± 0.014 | 1.082 ± 0.166 | 0.618 ± 0.126 | 0.463 ± 0.108 |
| | 20 | 0.139 ± 0.022 | 1.486 ± 0.305 | 0.847 ± 0.214 | 0.639 ± 0.168 |
| | 25 | 0.138 ± 0.043 | 1.475 ± 0.514 | 0.836 ± 0.317 | 0.641 ± 0.247 |
| | 30 | 0.143 ± 0.037 | 1.528 ± 0.338 | 0.869 ± 0.242 | 0.658 ± 0.201 |
| | 35 | 0.135 ± 0.053 | 1.447 ± 0.538 | 0.829 ± 0.326 | 0.624 ± 0.258 |
| LM-IR | 1 min | 0.398 ± 0.026 | 3.677 ± 0.287 | 2.046 ± 0.219 | 1.631 ± 0.204 |

depressions and intricate details of the mold surface before it solidifies. Consequently, the surface of the molded part becomes smoother as it better conforms to the smooth mold surface.

The roughness results showed that the LM-IR sample had higher roughness values than both HM(35) and LM, with Ra, Rz, Rv, and Rp values of 0.398 ± 0.026 μm, 3.677 ± 0.287 μm, 2.046 ± 0.219 μm, and 1.631 ± 0.204 μm, respectively. This behavior may be associated with structural rearrangement and additional crystallization in the near-surface region during annealing, which could contribute to greater local surface heterogeneity (Udagawa et al., 2016). Moreover, Fig. 9 (a–c) shows SEM images of the surface morphology of the HM(35), LM, and LM-IR samples. The SEM observations also qualitatively revealed differences in surface morphology, with the HM sample showing a more uniform and directional surface texture, whereas the LM and LM-IR samples exhibited more heterogeneous and irregular morphologies. Overall, the results suggest that surface roughness was governed by mold surface replication during molding and by the subsequent thermal history, with mold temperature affecting replication fidelity and IR annealing contributing to increased surface heterogeneity in the LM-IR sample.

### 3.4. Tensile properties and heat deflection temperature (HDT) evaluation

Fig. 10 shows the engineering stress-strain curves of specimens molded at mold temperatures of 30 °C and 100 °C, as well as specimens subjected to IR annealing. The specimen molded at 100 °C exhibited the highest modulus of elasticity, reaching 9310.6 MPa, whereas the LM and LM-IR samples showed values of 9072.6 and 9150.0 MPa, respectively. This behavior suggests that similar crystallinity levels did not necessarily lead to identical mechanical behavior, likely because the two processing routes generated different crystal morphologies (Tábi et al., 2016). The results also showed that specimens produced by low mold temperature molding exhibited the highest maximum stress, reaching 48.98 ± 0.42 MPa, whereas the samples crystallized in-mold and by IR annealing showed maximum stress values of 44.66 ± 1.44 MPa and 43.50 ± 0.83 MPa, respectively. This behavior is consistent with the higher crystallinity developed under these processing conditions, which reduced ductility and promoted earlier failure.

The results of the heat deflection temperature analysis revealed a significant increase in HDT following the crystallization treatments. The specimens produced under low mold temperature molding exhibited an HDT of 55.0 ± 0.2 °C, whereas substantially higher values were obtained

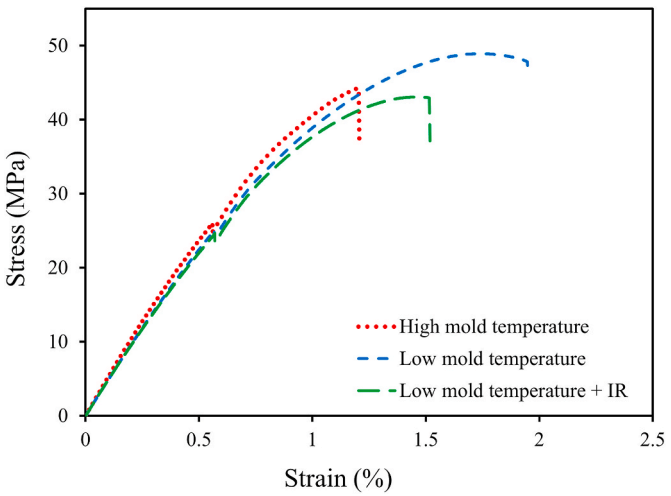


**Fig. 10.** Engineering stress-strain curves of dog-bone specimens molded under low mold temperature, low mold temperature followed by IR annealing, and high mold temperature molding.

for the specimens crystallized in-mold and by IR annealing, reaching 145.81 ± 0.42 °C and 134.6 ± 1.4 °C, respectively. This substantial increase in HDT indicates that the higher crystallinity developed under these processing conditions markedly improved the thermomechanical stability of PLA. Moreover, although HM and LM-IR exhibited comparable crystallinity values, the HDT of HM was higher than that of LM-IR. This difference could be due to differences in the crystalline structure developed during the two crystallization routes (Tábi et al., 2016).

### 3.5. Gate-to-gate energy and sustainability assessment

Table 3 summarizes the energy consumption per part for the two processing routes. The total energy per part was calculated using Equation (8):

$$E_{Total} = E_{Molding} + E_{IR} \tag{8}$$

As shown in Table 3, producing one HM(35) part required 8.86 ± 0.22 Wh/part at the press-only level, whereas molding one LM part required only 2.90 ± 0.08 Wh/part. This lower molding energy for the LM condition is attributed to the lower mold temperature used during

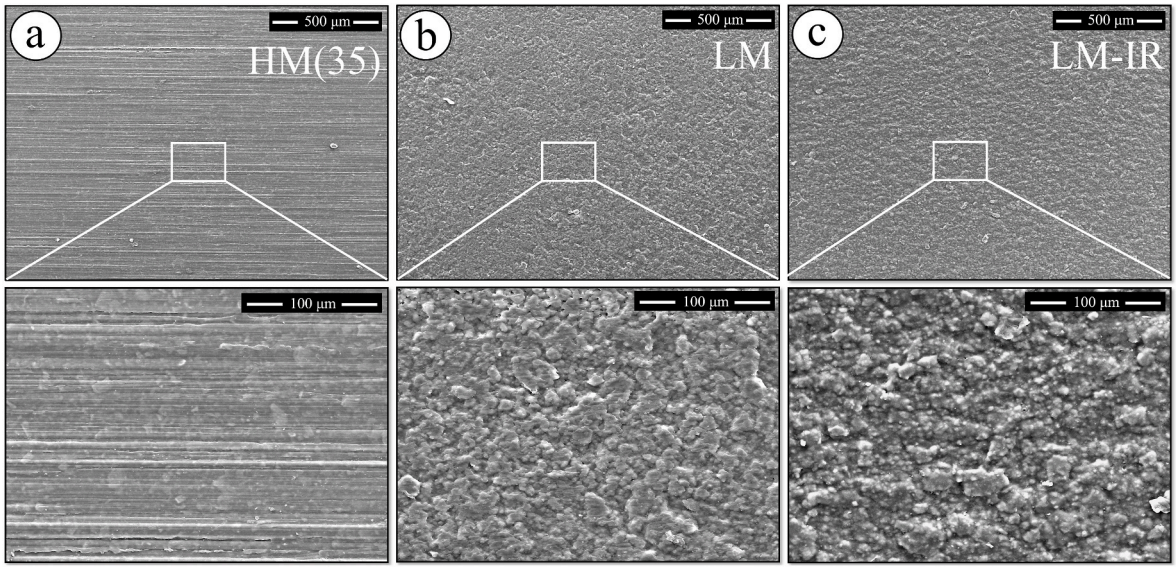


**Fig. 9.** SEM images of the surface morphology of (a) HM(35), (b) LM, and (c) LM-IR samples, together with their corresponding magnified images.

**Table 3**
Gate-to-gate per-part energy (press-only and IR-annealing) (mean ± SD).

| Indicators | HM(35) | LM | LM-IR N = 1 | LM-IR N = 5 | LM-IR N = 15 | LM-IR N = 30 |
|---|---|---|---|---|---|---|
| $E_{Molding}$ (Wh/part) | 8.86 ± 0.22 | 2.90 ± 0.08 | 2.90 ± 0.08 | 2.90 ± 0.08 | 2.90 ± 0.08 | 2.90 ± 0.08 |
| $E_{IR}$ (Wh/part) | - | - | 56.71 ± 0.06 | 11.34 ± 0.02 | 3.78 ± 0.03 | 1.89 ± 0.05 |
| $E_{Total}$ (Wh/part) | 8.86 ± 0.22 | 2.90 ± 0.08 | 59.61 ± 0.10 | 14.24 ± 0.08 | 6.68 ± 0.09 | 4.79 ± 0.09 |

**Note:** Values refer only to measured gate-to-gate electrical energy demand.

processing. Because the IR unit was operated at fixed power, distance, and heating time, the total energy consumed in one annealing run remained approximately constant. As a result, the IR energy per part depended strongly on the number of parts treated per run (*N*), since the total annealing energy was distributed among more samples. For a single-part IR annealing run ($N = 1$), the total energy demand ($E_{Molding} + E_{IR}$) was 59.61 ± 0.10 Wh/part. However, when the annealing chamber was more effectively utilized, the total energy decreased to 14.24 ± 0.08 Wh/part at $N = 5$, 6.68 ± 0.09 Wh/part at $N = 15$, and 4.79 ± 0.09 Wh/part at $N = 30$. Therefore, although the manufacturing of the LM-IR samples was initially more energy intensive at low batch size, it became more energy efficient than HM(35) when operated at the optimized capacity of $N = 30$ parts.

Table 4 presents the corresponding mass-specific sustainability indicators, including specific energy consumption (SEC), carbon footprint ($CO_2e$), and electricity cost. These values were obtained by normalizing the energy consumption to the processed mass, while $CO_2e$ and electricity cost were calculated from the total electricity consumption using the corresponding conversion factors. As expected from the energy results in Table 3, the SEC values showed the same overall trend. The $SEC_{Molding}$ for the LM condition remained constant at 2.90 ± 0.08 kWh/kg, whereas the contribution of the IR step decreased markedly with increasing batch size. Consequently, the $SEC_{Total}$ for the LM-IR route decreased from 59.61 ± 0.10 kWh/kg at $N = 1$ to 4.79 ± 0.09 kWh/kg at $N = 30$, which is lower than the value obtained for HM(35) (8.86 ± 0.22 kWh/kg). This shows that the LM-IR route becomes energetically advantageous only when the IR annealing step is applied at sufficiently high batch utilization.

The same pattern was observed for $CO_2e$ and electricity cost, since both indicators are directly linked to electricity consumption. Increasing the annealing load from $N = 1$ to $N = 30$ reduced the carbon footprint from 17.88 ± 0.03 to 1.43 ± 0.03 kg/kg and the electricity cost from 11.79 ± 0.02 to 0.94 ± 0.02 €/kg. Consequently, relative to HM(35), the optimized LM-IR condition ($N = 30$) reduced SEC from 8.86 ± 0.22 to 4.79 ± 0.09 kWh/kg, $CO_2e$ from 2.64 ± 0.06 to 1.43 ± 0.03 kg/kg, and electricity cost from 1.74 ± 0.04 to 0.94 ± 0.02 €/kg, corresponding to reductions of approximately 45%.

These electricity-cost results should be interpreted within the same boundary as the energy analysis. They reflect only the variable electricity expenditure derived from the measured process energy and the selected tariff and, therefore, do not capture broader economic elements that may influence industrial adoption of the LM-IR route, such as capital investment for the IR unit, maintenance, equipment depreciation, labor, automation/handling, or floor-space-related overheads. Because these factors are strongly plant- and implementation-specific, they were not quantified in the present work. As a result, while the electricity-cost indicator suggests a potential operating-cost advantage for LM-IR under optimized utilization, it should not be interpreted as a complete economic evaluation or as direct evidence of lower total cost of ownership.

From a reduced-energy-processing perspective, the main difference between the two routes lies in how the thermal requirement for crystallization is delivered. In the HM route, crystallization is achieved inside the mold by maintaining a high mold temperature and longer cooling time, which increases the energy demand of the molding stage. In contrast, the LM-IR route reduces the energy demand during molding by using a low mold temperature and shorter cycle, while shifting crystallization to a short post-molding IR annealing step. Therefore, the energetic benefit of the LM-IR route arises from process decoupling, although its effectiveness depends on annealing time and utilization conditions. This comparison also shows that process decoupling is not merely an energy-management strategy: even when similar crystallinity is achieved, the selected route leads to different surface and thermo-mechanical outcomes and different practical constraints, meaning that route selection requires a combined process-property-energy perspective rather than crystallinity maximization alone. Overall, these results indicate that when comparable crystallinity is achieved, low mold temperature molding followed by IR annealing can represent a more sustainable processing route than direct in-mold crystallization under high mold temperature molding.

These conclusions should, however, be interpreted in light of the specific formulation investigated in this study. In particular, the present results were obtained for a single industrially relevant commercial PLA/talc compound (IM2368), and therefore the quantitative findings should be considered formulation-specific rather than directly generalizable to all PLA grades or nucleating systems. The material composition is expected to influence the balance between in-mold crystallization and post-molding IR annealing. In particular, talc content can affect crystallization kinetics because talc acts as an efficient heterogeneous nucleating agent for PLA. At lower talc loadings, the lower nucleation density would likely slow crystallization, potentially requiring longer residence times during the high mold temperature molding or longer IR annealing times to achieve the same crystallinity level. Conversely, higher talc contents may further accelerate crystallization and increase stiffness and heat resistance, but may also promote filler agglomeration, modify melt viscosity, and affect surface quality and tensile behavior. Likewise, differences among PLA grades, including molecular weight, are expected to affect chain mobility and crystallization kinetics, thereby influencing the absolute values of crystallinity, cooling and annealing times, mechanical response, and specific energy consumption. As a result, although the comparative trends identified here are useful for the investigated system, the exact crossover in performance and energy efficiency between the HM and LM-IR routes should not be assumed to occur under the same conditions for other PLA grades or

**Table 4**
Per-kg sustainability metrics under a gate-to-gate boundary: SEC, $CO_2e$, and electricity-cost indicator.

| Indicators | HM(35) | LM | LM-IR N = 1 | LM-IR N = 5 | LM-IR N = 15 | LM-IR N = 30 |
|---|---|---|---|---|---|---|
| **$SEC_{Molding}$ (kWh/kg)** | 8.86 ± 0.22 | 2.90 ± 0.08 | 2.90 ± 0.08 | 2.90 ± 0.08 | 2.90 ± 0.08 | 2.90 ± 0.08 |
| **$SEC_{IR}$ (kWh/kg)** | - | - | 56.71 ± 0.06 | 11.34 ± 0.02 | 3.78 ± 0.03 | 1.89 ± 0.05 |
| **$SEC_{Total}$ (kWh/kg)** | 8.86 ± 0.22 | 2.90 ± 0.08 | 59.61 ± 0.10 | 14.24 ± 0.08 | 6.68 ± 0.09 | 4.79 ± 0.09 |
| **$CO_2e$ (kg/kg)** | 2.64 ± 0.06 | 0.83 ± 0.02 | 17.88 ± 0.03 | 4.27 ± 0.02 | 2.00 ± 0.03 | 1.43 ± 0.03 |
| **Electricity cost (€/kg)** | 1.74 ± 0.04 | 0.55 ± 0.02 | 11.79 ± 0.02 | 2.81 ± 0.02 | 1.32 ± 0.02 | 0.94 ± 0.02 |

**Note:** Electricity cost refers only to variable electricity expenditure based on the selected tariff.

alternative nucleating systems.

In addition, the energy-related comparisons should be interpreted in light of the selected system boundary. The SEC, $CO_2e$, and electricity-cost values reported here refer to a gate-to-gate assessment and therefore do not include auxiliary and facility-level contributions such as compressed-air supply, material drying beyond the pre-drying step, machine start-up, or plant-wide electrical losses. Including these contributions would increase the absolute energy demand of both routes. Their relative effect may also depend on the industrial configuration, since drying demand, fixed auxiliary loads, and facility-level losses may be distributed differently depending on production scale, plant organization, and machine utilization. Therefore, the present results are most appropriate for comparing the two processing routes under the monitored operating conditions, whereas the absolute SEC values should not be interpreted as full-facility energy footprints. A cradle-to-gate LCA would broaden this interpretation by including upstream contributions such as compounding, material transport, pellet drying, and electricity generation. Comparing these upstream burdens with the measured gate-to-gate processing energy would help contextualize the present results within a broader sustainability framework.

The experimentally measured SEC values provide a direct comparison between HM, LM, and LM-IR under the present micro-injection molding conditions. However, because SEC is strongly affected by throughput and the mass over which fixed machine loads are distributed, the experimental values alone cannot indicate how the route comparison may evolve with increasing part size. Therefore, a simplified first-order scaling analysis is introduced to connect the measured SEC trends with the expected influence of part mass and process rate. The purpose of this analysis is qualitative and trend-based rather than predictive for full-scale industrial production. The behavior of power and SEC as a function of throughput in injection molding can be described by Equation (9) (Spiering et al., 2015; Thiriez and Gutowski, 2006):

$$P = P_0 + K\dot{m} \Rightarrow SEC = \frac{P}{\dot{m}} = \frac{P_0}{\dot{m}} + K \tag{9}$$

where $P$ is the total machine power, $P_0$ is the fixed power requirement (power required when the machine is on but not processing any polymer), $K$ is the processing constant, and $\dot{m}$ is the material throughput or process rate. According to Equation (9), the behavior of SEC for HM, LM, and LM-IR, along with the predicted trend of SEC as a function of part mass (which is directly proportional to $\dot{m}$), is shown in Fig. 11.

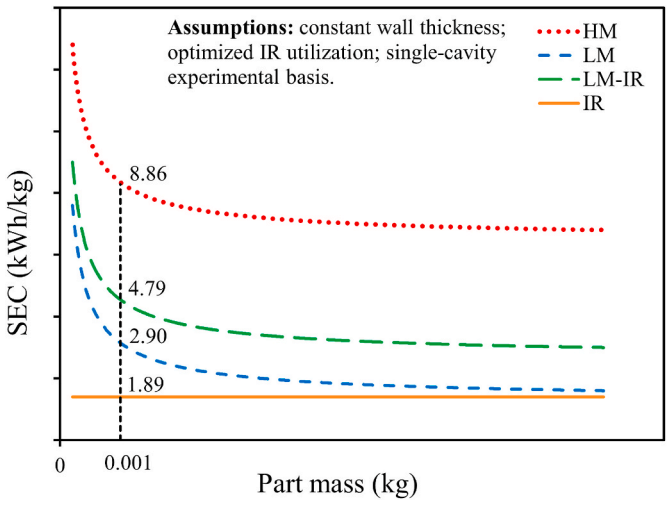


**Fig. 11.** SEC values for HM, LM-IR, LM, and IR, and first-order prediction as a function of part mass. (The scaling trends assume constant wall thickness and optimized IR utilization. Industrial extrapolation may be sensitive to cavity number, machine utilization, and synchronization between molding and annealing capacity.)

For the HM configuration, all injection parameters were identical to LM, and the additional energy required for mold heating shifted the HM curve upward, keeping it parallel to the LM trend, as illustrated in Fig. 11.

The total radiant energy emitted in the IR is described by the Stefan–Boltzmann law as:

$$E_{Emit} = \varepsilon\sigma T_s^4 A_{IR} t_{c,IR} \tag{10}$$

where $E_{Emit}$ is the total emitted energy, $\varepsilon$ is the emissivity of the heater surface, $\sigma$ is the Stefan-Boltzmann constant, $T_s$ is the heater-surface temperature, $A_{IR}$ is the emitting surface area, and $t_{c\text{-}IR}$ is the exposure time. In an optimized IR setup, the emitting surface area $A_{IR}$ scales proportionally with the total irradiated part surface ($A_{Part}$) to ensure uniform exposure ($A_{IR} \propto A_{Part}$). Since the part mass increases linearly with its surface area at constant thickness, both $E_{Emit}$ and $m$ scale proportionally with $A_{Part}$, yielding:

$$SEC_{IR} = \frac{E_{Emit}}{m} = \left(\frac{\varepsilon\sigma T_s^4 t_{c,IR}}{\rho t_h}\right)\left(\frac{A_{IR}}{A_{Part}}\right) = Constant \tag{11}$$

This relationship confirms that, under fixed IR heating temperature and exposure time, $SEC_{IR}$ remains constant as part mass increases, as illustrated in Fig. 11 by a flat curve across the part mass range. Additionally, the LM-IR configuration integrates LM injection molding with the annealing stage, resulting in a constant offset added to the LM curve, as shown in Fig. 11. The results showed that low mold temperature molding plus IR annealing consumed less energy than high mold temperature molding to achieve a similar degree of crystallinity for the investigated micro-scale parts. The first-order scaling analysis suggests that this comparison may remain qualitatively valid for larger parts within the gate-to-gate boundary and under the specific assumptions adopted here, particularly constant thickness, comparable utilization conditions, and optimized IR setup.

However, this extrapolation should be treated with caution because the experimental data were generated on parts with a mass of approximately 1 g, which is substantially lower than that of many industrial injection-molded components. At this scale, SEC is especially sensitive to fixed machine and tooling loads, low effective utilization, and the characteristics of the micro-injection molding platform. For larger industrial parts, the relative contribution of fixed loads, mold thermal inertia, cooling requirements, machine size, cavity number, part geometry, and thickness distribution may differ substantially. For example, cavity number can affect the distribution of fixed press and mold-heating loads over the produced mass per cycle, thereby shifting both the absolute SEC values and the crossover point between the HM and LM-IR routes. Therefore, Fig. 11 should be interpreted as a first-order, trend-based scaling exercise rather than as a direct quantitative prediction for full-scale industrial production.

From an industrial implementation perspective, however, the energetic advantage of the LM-IR route should be balanced against practical constraints that are not captured by the gate-to-gate SEC analysis alone. Although offline IR annealing decouples crystallization from the molding cycle, it also requires additional equipment footprint, intermediate part handling, and buffer storage between molding and post-treatment. In practice, the annealing station must be sized so that its effective capacity matches the output of the injection molding machine; otherwise, the shorter molding cycle obtained under the LM condition may not translate into a higher overall production rate, because part accumulation, waiting time before annealing, or additional logistics may create downstream bottlenecks. Moreover, the favorable energy values reported here for LM-IR were obtained under optimized batch utilization, whereas partially loaded industrial operation would increase the per-part annealing energy and reduce the practical advantage of this route. Therefore, the industrial scalability of LM-IR depends not only on the part-size trend of SEC, but also on floor-space availability, line integration strategy, batch-management efficiency, and throughput

synchronization between molding and annealing.

Additionally, to contextualize our results, we noted that the measured SEC of 8.86 ± 0.22 kWh/kg for the HM(35) and 2.90 ± 0.08 kWh/kg for the LM at the press-only level ($SEC_{Molding}$) are both higher than the commonly cited press-only range for all-electric machines (0.4-0.9 kWh/kg) (Thiriez and Gutowski, 2006). The elevated values are explained by the micro-injection scale (part mass ≈ 1 g), which yields low effective utilization, resulting in fixed press/tooling loads distributed over very little mass. This effect is captured by empirical SEC models (showing SEC high at low utilization and declining with increased throughput/efficiency) and is also evident in Fig. 11 (Masato et al., 2018; Spiering et al., 2015). In addition, mold temperature is a major contributor to the electricity use of injection molding machines (Thiriez and Gutowski, 2006). Thus, maintaining a high mold temperature at 100 °C introduces a continuous thermal load. As other studies show, reducing mold heating lowers per-part energy demand, consistent with our observations (Thiriez and Gutowski, 2006).

## 4. Conclusions

This study compared two processing approaches for producing highly crystalline PLA/talc composite parts by evaluating manufacturability, part quality, crystallinity, thermomechanical and mechanical properties, and specific energy performance. The two approaches were: (i) high mold temperature molding (HM), and (ii) low mold temperature molding followed by infrared (IR) post-molding annealing (LM-IR). The results showed that, while the crystallinity of the LM samples was only 25.0 ± 0.23%, high mold temperature molding promoted in-mold crystallization up to 54.12 ± 0.65%, which was the highest crystallinity achieved for the studied material, and also improved surface quality, although at the expense of longer cycle times due to the 35 s residence time inside the mold. In contrast, molding at low mold temperature enabled faster part production, although the resulting parts exhibited lower crystallinity and rougher surfaces. However, a short IR post-treatment of 1 min effectively compensated for the limited crystallization achieved under low mold temperature molding, allowing LM-IR parts to reach crystallinity comparable to HM(35). The higher crystallinity achieved through both HM(35) and LM-IR was also reflected in significantly enhanced heat deflection temperature (HDT). In particular, HDT increased from 55.0 ± 0.2 °C for the LM sample to 145.81 ± 0.42 °C and 134.6 ± 1.4 °C for HM(35) and LM-IR, respectively, confirming the strong influence of crystallinity and processing route on the final thermal performance of the parts. Taken together, these findings indicate that comparable crystallinity obtained via HM and LM-IR does not imply equivalent processability or final-part performance. The main contribution of the present work is therefore the integrated quantification of the resulting process-property-energy trade-offs between two established routes for manufacturing highly crystalline PLA/talc parts.

Within the gate-to-gate boundary considered in this work, LM-IR achieved 45% lower specific energy consumption per unit mass of processed material than high mold temperature molding, together with proportional reductions in associated $CO_2e$ emissions and electricity cost. However, these values reflect the monitored gate-to-gate process energy only, and the reported cost indicator is limited to electricity expenditure. Accordingly, they do not include auxiliary services or facility-level losses, nor broader economic factors such as capital expenditure, maintenance, equipment depreciation, labor, and handling associated with implementing an additional IR annealing step or upstream environmental burdens outside the gate-to-gate boundary. These aspects are beyond the scope of the present study and would need to be considered in future cradle-to-gate LCA and industrial-scale techno-economic assessments to contextualize the findings for broader sustainability interpretation.

In addition, the first-order scaling analysis suggested that, under optimized IR setup and utilization conditions and at constant thickness, LM-IR may remain energetically favorable as part size increases. However, because the experimental SEC values were obtained on micro-injected parts with a mass of approximately 1 g, this extrapolation should be interpreted cautiously and as trend-indicative rather than as a direct quantitative prediction for typical industrial injection-molded components. Moreover, because only one commercial PLA/talc formulation was investigated, further validation across PLA grades with different molecular weights, stereochemical compositions, and nucleating-agent contents is needed before extending the quantitative conclusions to other systems.

The practical benefits of the low mold temperature molding followed by post-molding IR annealing route are expected to depend on careful control of the IR heating conditions, adequate annealing-unit utilization, sufficient floor-space availability, effective integration of the annealing step with molding and handling operations, and further validation for more complex geometries and different thicknesses. In particular, the shorter molding cycle achieved under the LM condition does not automatically translate into higher line productivity unless the downstream IR stage is properly dimensioned to avoid bottlenecks, excessive intermediate storage, and throughput losses. Nevertheless, beyond the direct process comparison, the present results demonstrate the applicability of this route for manufacturing thin-wall PLA/talc parts requiring increased crystallinity and improved thermomechanical stability. More broadly, the study provides useful guidance for the selection of reduced-energy processing strategies for the investigated PLA/talc formulation and, more cautiously, for similar nucleated PLA components at constant thickness.

Future work should systematically examine the effect of formulation variables, particularly talc loading, PLA molecular weight, and other nucleating systems, on crystallization kinetics, final morphology, and process-energy balance. Such a study would help establish the extent to which the trends observed here remain valid across different PLA compounds and industrial grades. Such future work could also include dedicated crystallization-kinetics modeling (e.g., Avrami-type analysis under appropriate controlled conditions or alternative non-isothermal approaches) to move from the qualitative trends reported here toward predictive capability. Future work should also combine Moldflow analysis with direct temperature measurements, such as embedded thermocouples or IR thermography, in order to quantitatively validate the predicted thermal histories during molding and demolding.

Alternative annealing technologies also merit investigation, such as microwave heating as a potential post-molding annealing method. Although its specific effects in this context remain to be clarified, it may offer potential processing advantages and is therefore worthy of further investigation. Moreover, although nucleating agents such as talc are effective in accelerating PLA crystallization and promoting homocrystal formation, PLA stereocomplexation represents another promising strategy, since it can lead to the formation of stereocomplex crystals with higher thermal stability than conventional homocrystals (Bai et al., 2017; Guo et al., 2022; Tan et al., 2016). Investigating these approaches in terms of energy consumption, manufacturability, crystallinity, and thermomechanical performance may further extend the applicability of PLA-based parts under more demanding service conditions and will be addressed in future work.

## Ethical compliance

All procedures performed in this study involving human participants were in accordance with the ethical standards of the institutional and/or national research committee and the 1964 Helsinki Declaration and its later amendments or comparable ethical standards.

## Declaration of generative AI and AI-assisted technologies in the writing process

During the preparation of this work, the authors used Chat GPT 5.1 in order to improve the level of English writing. After using this tool/

service, the authors reviewed and edited the content as needed and take full responsibility for the content of the published article.

## Funding

This project was funded by the European Union's Horizon 2021 research and innovation program under the Marie Skłodowska-Curie grant agreement No. 101072846 (SERENADE).

## CRediT authorship contribution statement

**Hadi Saniei:** Data curation, Investigation, Software, Visualization, Writing – original draft. **Alberto Marcolongo:** Conceptualization, Supervision, Validation, Writing – review & editing. **Marco Sorgato:** Supervision, Validation, Writing – review & editing. **Giovanni Lucchetta:** Conceptualization, Project administration, Supervision, Validation, Writing – review & editing.

## Declaration of competing interest

The authors declare the following financial interests/personal relationships which may be considered as potential competing interests: HADI SANIEI reports financial support was provided by European Commission Marie Sklodowska-Curie Actions (SERENADE). If there are other authors, they declare that they have no known competing financial interests or personal relationships that could have appeared to influence the work reported in this paper.

## Data availability

Data will be made available on request.

## References

Bai, H., Deng, S., Bai, D., Zhang, Q., Fu, Q., 2017. Recent advances in processing of stereocomplex-type polylactide. Macromol. Rapid Commun. 38. https://doi.org/10.1002/marc.201700454.

Balaras, C.A., Dascalaki, E.G., Patsioti, M., Droutsa, K.G., Kontoyiannidis, S., Cholewa, T., 2023. Carbon and greenhouse gas emissions from electricity consumption in European union buildings. Buildings 14, 71. https://doi.org/10.3390/buildings14010071.

Bergström, J.S., Hayman, D., 2016. An overview of mechanical properties and material modeling of polylactide (PLA) for medical applications. Ann. Biomed. Eng. 44, 330–340. https://doi.org/10.1007/s10439-015-1455-8.

Butt, J., Bhaskar, R., 2020. Investigating the effects of annealing on the mechanical properties of FFF-printed thermoplastics. J. Manuf. Mater. Process. 4, 38. https://doi.org/10.3390/jmmp4020038.

Cheng, Q., Yuan, Y., Sun, H., Gu, P., Wang, D., Zhang, L., Xia, W., Wang, Y., Zhou, H., 2025. Rapid energy-efficient manufacturing of high-performance glass fiber reinforced polymer composites via infrared radiation. Eng. Fract. Mech. 320, 111063. https://doi.org/10.1016/J.ENGFRACMECH.2025.111063.

Costa, A.R. de M., Luna, C.B.B., do Nascimento, E.P., Ferreira, E. da S.B., Costa, C. de M., de Almeida, Y.M.B., Araújo, E.M., 2023. Tailoring PLA/ABS blends compatibilized with SEBS-g-MA through annealing heat treatment. Polymers (Basel) 15, 3434. https://doi.org/10.3390/polym15163434.

De Santis, F., Volpe, V., Pantani, R., 2017. Effect of molding conditions on crystallization kinetics and mechanical properties of poly(lactic acid). Polym. Eng. Sci. 57, 306–311. https://doi.org/10.1002/pen.24414.

de Souza Marconi, P.G.C., Beal, V.E., Ferreira, C.V., Ribeiro, A.S., 2025. Systematic approach for injection mold rapid tooling. Int. J. Adv. Manuf. Technol. 141, 5681–5696. https://doi.org/10.1007/s00170-025-17024-2.

Deng, X., Xiang, W., Lin, W., Zheng, Z., Yang, Y., 2025. Few-shot injection molding quality prediction method integrating deep transfer and multi-task learning. Int. J. Adv. Manuf. Technol. 141, 609–632. https://doi.org/10.1007/s00170-025-16651-z.

Doroudiani, S., Park, C.B., Kortschot, M.T., 1996. Effect of the crystallinity and morphology on the microcellular foam structure of semicrystalline polymers. Polym. Eng. Sci. 36, 2645–2662. https://doi.org/10.1002/pen.10664.

Elduque, A., Elduque, D., Pina, C., Clavería, I., Javierre, C., 2018. Electricity consumption estimation of the polymer material injection-molding manufacturing process: empirical model and application. Materials 11, 1740. https://doi.org/10.3390/ma11091740.

Fambri, L., Migliaresi, C., 2022. Crystallization and thermal properties. In: Poly(Lactic Acid). Wiley, pp. 135–151. https://doi.org/10.1002/9781119767480.ch8.

Farah, S., Anderson, D.G., Langer, R., 2016. Physical and mechanical properties of PLA, and their functions in widespread applications — a comprehensive review. Adv. Drug Deliv. Rev. 107, 367–392. https://doi.org/10.1016/j.addr.2016.06.012.

Feng, Y., Ma, P., Xu, P., Wang, R., Dong, W., Chen, M., Joziasse, C., 2018. The crystallization behavior of poly(lactic acid) with different types of nucleating agents. Int. J. Biol. Macromol. 106, 955–962. https://doi.org/10.1016/j.ijbiomac.2017.08.095.

Fischer, E.W., Sterzel, H.J., Wegner, G., 1973. Investigation of the structure of solution grown crystals of lactide copolymers by means of chemical reactions. Kolloid-Zeitschrift und Zeitschrift für Polymere 251, 980–990. https://doi.org/10.1007/BF01498927.

Gao, P., Masato, D., 2024. The effects of nucleating agents and processing on the crystallization and mechanical properties of polylactic acid: a review. Micromachines (Basel) 15, 776. https://doi.org/10.3390/mi15060776.

Gülçür, M., Rich, A., Griffiths, O., Wilson, P., Williams, M., Gibbons, G., 2025. Rapid tooling: comparative analysis of mechanical properties and energy efficiency in micro-injection mouldings using polymer and metal moulds. Manuf. Lett. 45, 31–35. https://doi.org/10.1016/J.MFGLET.2025.06.204.

Guo, M., Wu, Wenjing, Wu, Weixin, Gao, Q., 2022. Competitive mechanism of stereocomplexes and homocrystals in high-performance symmetric and asymmetric poly(lactic acid) enantiomers: qualitative methods. ACS Omega 7, 41412–41425. https://doi.org/10.1021/acsomega.2c05198.

Helanto, K., Talja, R., Rojas, O.J., 2021. Talc reinforcement of polylactide and biodegradable polyester blends via injection-molding and pilot-scale film extrusion. J. Appl. Polym. Sci. 138. https://doi.org/10.1002/app.51225.

Ivey, M., Melenka, G.W., Carey, JasonP., Ayranci, C., 2017. Characterizing short-fiber-reinforced composites produced using additive manufacturing. Adv. Manuf. Polym. Compos. Sci. 3, 81–91. https://doi.org/10.1080/20550340.2017.1341125.

Jain, S., Misra, M., Mohanty, A.K., Ghosh, A.K., 2012. Thermal, mechanical and rheological behavior of poly(lactic acid)/Talc composites. J. Polym. Environ. 20, 1027–1037. https://doi.org/10.1007/s10924-012-0500-z.

Jiang, L., Shen, T., Xu, P., Zhao, X., Li, X., Dong, W., Ma, P., Chen, M., 2016. Crystallization modification of poly(lactide) by using nucleating agents and stereocomplexation. e-Polymers 16, 1–13. https://doi.org/10.1515/epoly-2015-0179.

Kashyap, S., Datta, D., 2015. Process parameter optimization of plastic injection molding: a review. Int. J. Plast. Technol. 19, 1–18. https://doi.org/10.1007/s12588-015-9115-2.

Kitayama, S., Yamaya, K., Yamazaki, Y., Kubo, Y., Aiba, S., 2025. Process parameters optimization for minimizing warpage and cycle time using vibration-assisted plastic injection molding. Int. J. Adv. Manuf. Technol. 139, 3711–3722. https://doi.org/10.1007/s00170-025-16127-0.

Kocabey Çiftçi, P., Özceylan, E., 2025. A practical framework for corporate carbon footprint analysis: a case of emission sources, data collection, and calculations, in carpet industry. Clim. Change 178, 135. https://doi.org/10.1007/s10584-025-03981-w.

Kolstad, J.J., 1996. Crystallization kinetics of poly(L-lactide-co-meso-lactide). J. Appl. Polym. Sci. 62, 1079–1091. https://doi.org/10.1002/(SICI)1097-4628(19961114)62:7<1079::AID-APP14>3.0.CO;2-1.

Kuo, C.-C., Farooqui, A., Tasi, C.-X., Pan, X.-Y., Huang, S.-H., 2025. Revolutionizing metal powder injection molding: a cost-effective approach to tooling innovation. J. Manuf. Process. 150, 900–913. https://doi.org/10.1016/j.jmapro.2025.07.008.

Kuo, C.-C., Lin, P.-H., Xu, J.-Y., Lin, Z.-X., Wang, Z.-H., Huang, S.-H., 2024. Polymeric advancements in innovating wax injection molds using aluminum-filled epoxy resin with face-cooled waterfall cooling channels. J. Manuf. Process. 124, 954–965. https://doi.org/10.1016/j.jmapro.2024.06.065.

Lee, C., Pang, M.M., Koay, S.C., Choo, H.L., Tshai, K.Y., 2020. Talc filled polylactic-acid biobased polymer composites: tensile, thermal and morphological properties. SN Appl. Sci. 2, 354. https://doi.org/10.1007/s42452-020-2172-y.

Lee, J.E., Park, S.J., Son, Y., Park, K., Park, S.H., 2021. Mechanical reinforcement of additive-manufactured constructs using in situ auxiliary heating process. Addit. Manuf. 43, 101995. https://doi.org/10.1016/J.ADDMA.2021.101995.

Li, H., Huneault, M.A., 2007. Effect of nucleation and plasticization on the crystallization of poly(lactic acid). Polymer (Guildf). 48, 6855–6866. https://doi.org/10.1016/j.polymer.2007.09.020.

Lim, L.T., Auras, R., Rubino, M., 2008. Processing technologies for poly(lactic acid). Prog. Polym. Sci. 33, 820–852. https://doi.org/10.1016/J.PROGPOLYMSCI.2008.05.004.

Lucchetta, G., Masato, D., Sorgato, M., 2018. Optimization of mold thermal control for minimum energy consumption in injection molding of polypropylene parts. J. Clean. Prod. 182, 217–226. https://doi.org/10.1016/J.JCLEPRO.2018.01.258.

Maciariello, F., 2024. Analysis of the effect of draft angle and surface roughness on ejection forces in micro injection molding, 2686–2694. https://doi.org/10.21741/9781644903131-294.

Masato, D., Sorgato, M., Lucchetta, G., 2018. Effect of ultrasound vibration on the ejection friction in microinjection molding. Int. J. Adv. Manuf. Technol. https://doi.org/10.1007/s00170-018-1652-3.

Masato, D., Sorgato, M., Lucchetta, G., 2021. A new approach to the evaluation of ejection friction in micro injection molding. J. Manuf. Process. 62, 28–36. https://doi.org/10.1016/J.JMAPRO.2020.12.032.

Mileva, D., Tranchida, D., Gahleitner, M., 2018. Designing polymer crystallinity: an industrial perspective. Polym. Cryst. 1. https://doi.org/10.1002/pcr2.10009.

Moshood, T.D., Nawanir, G., Mahmud, F., Mohamad, F., Ahmad, M.H., AbdulGhani, A., 2022. Sustainability of biodegradable plastics: new problem or solution to solve the global plastic pollution? Curr. Res. Green Sustain. Chem. 5, 100273. https://doi.org/10.1016/j.crgsc.2022.100273.

Nagarajan, V., Mohanty, A.K., Misra, M., 2016. Perspective on polylactic acid (PLA) based sustainable materials for durable applications: focus on toughness and heat

resistance. ACS Sustain. Chem. Eng. 4, 2899–2916. https://doi.org/10.1021/acssuschemeng.6b00321.
Nofar, M., Zhu, W., Park, C.B., Randall, J., 2011. Crystallization kinetics of Linear and long-chain-branched polylactide. Ind. Eng. Chem. Res. 50, 13789–13798. https://doi.org/10.1021/ie2011966.
Oubellaouch, K., Pelaccia, R., Orazi, L., Pozzi, P., Carmignato, S., Bonato, N., Donati, L., Raimondi, L., Reggiani, B., 2025. A novel experimental–numerical procedure for the rheological characterization of thermoplastic polymers applied to injection molding. Int. J. Adv. Manuf. Technol. 140, 5419–5433. https://doi.org/10.1007/s00170-025-16522-7.
P, W.B., O, V.C., n.d. Swiss Centre for Life Cycle Inventories Overview and Methodology (Final) Acknowledgements v3.
Pontes, A.J., Pouzada, A.S., 2004. Ejection force in tubular injection moldings. Part I: effect of processing conditions. Polym. Eng. Sci. 44, 891–897. https://doi.org/10.1002/pen.20080.
Psomopoulos, C.S., Skoula, I., Karras, C., Chatzimpiros, A., Chionidis, M., 2010. Electricity savings and $CO_2$ emissions reduction in buildings sector: how important the network losses are in the calculation? Energy 35, 485–490. https://doi.org/10.1016/J.ENERGY.2009.10.016.
Rehman, M.M. ur, Evens, T., Vanwersch, P., Van Bael, A., Castagne, S., 2025. Development of extreme wettable/non-wettable polymeric surfaces through injection molding replication of femtosecond laser-induced micro and nano textures. Int. J. Adv. Manuf. Technol. 140, 6729–6744. https://doi.org/10.1007/s00170-025-16641-1.
Rojas, A., Velásquez, E., Patiño Vidal, C., Guarda, A., Galotto, M.J., López de Dicastillo, C., 2021. Active PLA packaging films: effect of processing and the addition of natural antimicrobials and antioxidants on physical properties, release kinetics, and compostability. Antioxidants 10, 1976. https://doi.org/10.3390/antiox10121976.
Saeidlou, S., Huneault, M.A., Li, H., Park, C.B., 2012. Poly(lactic acid) crystallization. Prog. Polym. Sci. 37, 1657–1677. https://doi.org/10.1016/j.progpolymsci.2012.07.005.
Seok, W., Jeon, E., Kim, Y., 2023. Effects of annealing for strength enhancement of FDM 3D-Printed ABS reinforced with recycled carbon fiber. Polymers (Basel) 15, 3110. https://doi.org/10.3390/polym15143110.
Shakoor, A., Thomas, N.L., 2014. Talc as a nucleating agent and reinforcing filler in poly (lactic acid) composites. Polym. Eng. Sci. 54, 64–70. https://doi.org/10.1002/pen.23543.
Singh, N., Ogunseitan, O.A., Wong, M.H., Tang, Y., 2022. Sustainable materials alternative to petrochemical plastics pollution: a review analysis. Sustainable Horizons 2, 100016. https://doi.org/10.1016/j.horiz.2022.100016.
Singh, G., Verma, A., 2017. A brief review on injection moulding manufacturing process. Mater. Today Proc. 4, 1423–1433. https://doi.org/10.1016/J.MATPR.2017.01.164.
Sorgato, M., Masato, D., Lucchetta, G., 2017. Effects of machined cavity texture on ejection force in micro injection molding. Precis. Eng. 50, 440–448. https://doi.org/10.1016/J.PRECISIONENG.2017.06.019.
Spiering, T., Kohlitz, S., Sundmaeker, H., Herrmann, C., 2015. Energy efficiency benchmarking for injection moulding processes. Robot. Comput. Integrated Manuf. 36, 45–59. https://doi.org/10.1016/J.RCIM.2014.12.010.
Spierling, S., Knüpffer, E., Behnsen, H., Mudersbach, M., Krieg, H., Springer, S., Albrecht, S., Herrmann, C., Endres, H.-J., 2018. Bio-based plastics - a review of environmental, social and economic impact assessments. J. Clean. Prod. 185, 476–491. https://doi.org/10.1016/j.jclepro.2018.03.014.
Sudin, M.N., 2024. Effect of annealing parameters on surface roughness and tensile stress of 3D-Printed ABS parts. El-Cezeri Fen ve Mühendislik Dergisi. https://doi.org/10.31202/ecjse.1369831.
Swetha, T.A., Ananthi, V., Bora, A., Sengottuvelan, N., Ponnuchamy, K., Muthusamy, G., Arun, A., 2023a. A review on biodegradable polylactic acid (PLA) production from fermentative food waste - its applications and degradation. Int. J. Biol. Macromol. 234, 123703. https://doi.org/10.1016/j.ijbiomac.2023.123703.
Swetha, T.A., Bora, A., Mohanrasu, K., Balaji, P., Raja, R., Ponnuchamy, K., Muthusamy, G., Arun, A., 2023b. A comprehensive review on polylactic acid (PLA) – synthesis, processing and application in food packaging. Int. J. Biol. Macromol. 234, 123715. https://doi.org/10.1016/j.ijbiomac.2023.123715.
Taib, N.A.A.B., Rahman, M.R., Huda, D., Kuok, K.K., Hamdan, S., Bakri, M.K.B., Julaihi, M.R.M.B., Khan, A., 2023. A review on poly lactic acid (PLA) as a biodegradable polymer. Polym. Bull. 80, 1179–1213. https://doi.org/10.1007/s00289-022-04160-y.
Tan, B.H., Muiruri, J.K., Li, Z., He, C., 2016. Recent progress in using stereocomplexation for enhancement of thermal and mechanical property of polylactide. ACS Sustain. Chem. Eng. 4, 5370–5391. https://doi.org/10.1021/acssuschemeng.6b01713.
Tábi, T., Hajba, S., Kovács, J.G., 2016. Effect of crystalline forms (α′ and α) of poly(lactic acid) on its mechanical, thermo-mechanical, heat deflection temperature and creep properties. Eur. Polym. J. 82, 232–243. https://doi.org/10.1016/j.eurpolymj.2016.07.024.
Thiriez, A., Gutowski, T., 2006. An environmental analysis of injection molding. In: Proceedings of the 2006 IEEE International Symposium on Electronics and the Environment, 2006. IEEE, pp. 195–200. https://doi.org/10.1109/ISEE.2006.1650060.
Trivedi, A.K., Gupta, M.K., Singh, H., 2023. PLA based biocomposites for sustainable products: a review. Adv. Ind. Eng. Polym. Res. 6, 382–395. https://doi.org/10.1016/j.aiepr.2023.02.002.
Udagawa, A., Fujie, T., Kawamoto, Y., Saito, A., Takeoka, S., Asahi, T., 2016. Interfacial effects on the crystallization and surface properties of poly(l-lactic acid) ultrathin films. Polym. J. 48, 157–161. https://doi.org/10.1038/pj.2015.95.
Wach, R.A., Wolszczak, P., Adamus-Wlodarczyk, A., 2018. Enhancement of mechanical properties of FDM-PLA parts via thermal annealing. Macromol. Mater. Eng. 303. https://doi.org/10.1002/mame.201800169.
Wang, L., Wang, Y., Huang, Z., Weng, Y., 2015. Heat resistance, crystallization behavior, and mechanical properties of polylactide/nucleating agent composites. Materials & Design (1980-2015) 66, 7–15. https://doi.org/10.1016/j.matdes.2014.10.011.
Wang, T., Xia, L., Ni, M., Pan, S., Luo, C., 2024. Fundamentals of infrared heating and their application in thermosetting polymer curing: a review. Coatings 14, 875. https://doi.org/10.3390/coatings14070875.
Yu, F., Liu, T., Zhao, X., Yu, X., Lu, A., Wang, J., 2012. Effects of talc on the mechanical and thermal properties of polylactide. J. Appl. Polym. Sci. 125. https://doi.org/10.1002/app.36260.
Zhao, X., Yu, J., Liang, X., Huang, Z., Li, J., Peng, S., 2023. Crystallization behaviors regulations and mechanical performances enhancement approaches of polylactic acid (PLA) biodegradable materials modified by organic nucleating agents. Int. J. Biol. Macromol. 233, 123581. https://doi.org/10.1016/j.ijbiomac.2023.123581.